Materials Advances

ROYAL SOCIETY OF CHEMISTRY

PAPER

View Article Online
View Journal | View Issue

Cite this: *Mater. Adv.*, 2026, 7, 289

Ion implantation of magnesium guests into type II silicon clathrate films: an alternate approach to doping a cage-like silicon allotrope

Joseph P. Briggs, [ab] Sam Saiter, [c] Michael Walker, [c] Shei S. Su, [d] Michael Titze, [de] Yongqiang Wang, [f] Yinan Liu,[a] Reuben T. Collins, [c] Meenakshi Singh [c] and Carolyn A. Koh *[a]

Type II silicon clathrates, with their unique cage-like structure, offer exciting potential for applications in thermoelectrics, photovoltaics, and quantum materials due to their tunable electronic and thermal properties. This study investigates the use of ion implantation to introduce targeted guest atoms, which act as dopants, into type II Si clathrate films. The focus is on Mg as a test case for implantation, a dopant previously unreported in type II Si clathrates. The effects of ion implantation on the metastable Si clathrate structure were examined through systematic investigation of implant parameters. Time-of-flight secondary ion mass spectrometry depth profiling confirmed the successful implantation of Mg, while X-ray diffraction and confocal Raman spectroscopy demonstrated minimal structural damage at lower fluences, with the clathrate framework retaining its integrity without converting to other phases. At the higher end of the fluence range implantation caused localized transitions from clathrate to amorphous silicon. Implant activation using rapid thermal annealing was examined with the clathrate structure stable up to 500 °C and being converted to diamond silicon above this temperature. Post-implantation and activation structural characterization showed evidence of damage reversal. Electron paramagnetic resonance studies provided indirect evidence of dopant incorporation. These findings establish a foundation for introducing alternative guests/dopants into the Si clathrate cages through ion implantation, advancing their tunability for next-generation quantum and optoelectronic devices.

Received 6th June 2025,
Accepted 25th October 2025

DOI: 10.1039/d5ma00603a

rsc.li/materials-advances

Introduction

Silicon clathrates are metastable crystalline Si allotropes composed of silicon atoms arranged in a cage-like structure.[1,2] While the clathrates have the same sp^3 silicon bonding as traditional diamond cubic silicon (d-Si), the less dense geometry of clathrates allows for the encapsulation of "guest" atoms sitting in the interstitial spaces inside of the Si cages. Most synthesis approaches lead to guest atoms in the cages, which facilitate the structural transition to clathrates and tend to stabilize the expanded lattice structure. In clathrate literature the cage occupants are typically referred to as guest atoms, but can be viewed as donor atoms, since they tend to donate their valence electron to the crystalline Si framework. The structures of clathrates and other Si allotropes are detailed further in ref. 3. Whereas removal of guests has not been shown in the type I Si clathrates (M_8Si_{46}, with M representing the guest), the larger cages of type II (M_xSi_{136}, $0 < x \leq 24$) allow for the removal of the guests passing through the six member rings allowing for their occupation to be tuned.[4] Silicon clathrates were first identified as candidates for thermoelectrics due to their potential for low thermal conductivity combined with high electrical conductivity,[5–9] but more recently their bandgap tunability and defect engineering have made them attractive as emerging electronic materials.[10–13] This ability to manipulate their structural and electronic characteristics has made Si clathrates promising materials for a wide range of advanced applications, in optoelectronics,[14,15] photovoltaics,[12,16,17] batteries,[18–20] superconductors,[21,22] and spintronics,[23] and led to their consideration in emerging fields like energy storage and biomedical applications.[3]

What makes type II Si clathrates particularly interesting is their ability to support a range of guests inside their cages and

[a] *Department of Chemical and Biological Engineering, Colorado School of Mines, Golden, Colorado, 80401, USA. E-mail: ckoh@mines.edu*
[b] *Department of Chemistry and Biochemistry, University of California San Diego, San Diego, California, 92093, USA*
[c] *Department of Physics, Colorado School of Mines, Golden, Colorado, 80401, USA*
[d] *Sandia National Laboratories, Albuquerque, New Mexico, 87123, USA*
[e] *Instrumentation for Nano-Analytics, Luxembourg Institute of Science and Technology, 41 Rue Du Brill, Belvaux, L-4422, Luxembourg*
[f] *Los Alamos National Laboratory, Los Alamos, New Mexico, 87545, USA*

ability to tune their occupancy to influence their properties.[6,10,20] The most common route to synthesizing Si clathrates is through thermal decomposition of a M_4Si_4 Zintl phase precursor.[1,11,24–26] While a broad range of guest atoms are of interest in tuning the properties of clathrates, only a few guests, like Na, K, and Rb, have been demonstrated in this way.[2,25] Alternative means of incorporating novel guests have been explored with some success. These include electrochemical insertion, high pressure high temperature (HPHT) synthesis, spark plasma sintering (SPS), and thermal diffusion into already-formed near guest free Si clathrates.[19,20,27,28] However, these methods still have only shown incorporation of a few additional elements and still have restrictions on tunability of guest concentration. To realize the full potential of these Si allotropes, other guest introduction methods need to be explored. Often after synthesis, the guest/donor concentration is high ($x > 8$) and the clathrate exhibits metallic behavior.[29,30] If, however, the guest concentration can be reduced into the range of semiconductor dopants ($x \ll 1$), then the guest can be thought of as an interstitial dopant located inside the cages and the clathrate becomes a silicon-based semiconducting material with interesting optoelectronic properties that differ from those of d-Si.[11] In the present study, we focus on this low guest concentration regime where the implanted species can be viewed as a dopant. For the rest of the paper, we will tend to refer to the implanted species as a dopant unless the guest-like nature is important to the discussion.

Ion implantation offers a unique approach to incorporating alternative dopants and enhancing the properties of Si clathrates. It does this by offering flexibility in dopant choice and density, which then influences carrier density, both limitations of other techniques. This method involves bombarding the material with high-energy ions, which penetrate into the crystal lattice and alter its electronic and structural properties.[31–34] Ion implantation has been widely used in semiconductors, and especially d-Si, to introduce dopants like B and P with great spatial, depth, and dopant concentration control to tune optoelectronic and quantum properties and for fabrication of complementary metal–oxide-semiconductors (CMOS).[33,35–41] There has been limited work on implantation of clathrates with recent reporting of successful doping of type II clathrates with P, B, and As to introduce substitutional lattice species.[12] In the context of the present work, ion implantation in Si clathrates is particularly intriguing not only for the potential to selectively dope, but also the ability to incorporate alternative dopants not possible through current techniques. However, introducing new dopants and the effects of ion implantation on the stability and performance of clathrate structures remains virtually unexplored. Properties like defect formation, phase transitions, dopant activation, and material recovery through annealing need to be examined.

This study explores the impacts of broad beam and focused beam ion implantation on type II Si clathrate films, emphasizing both structural stability of the metastable clathrate film and dopant incorporation. Broad beam (BB) ion implantation involves the uniform implantation of a large area of film, while focused ion beam (FIB) implantation techniques enable things like a localized dopant based qubit in a specific device.[42,43] Magnesium ions were chosen as the primary implant species for this study since Mg is a potentially interesting dopant from column II which has not yet been incorporated in Si clathrates in any other way. Additionally, preliminary FIB implantation of Li ions was performed to study the effects of the implant ion size. The focus of this paper, however, is on implantation itself and whether it can be an effective technique for introducing alternative dopants. With d-Si, dopant implantation is typically followed by annealing to activate the dopant and repair damage caused by the implant. Such annealing, however, typically occurs at temperatures (*i.e.* > 1000 °C)[44] well above where the metastable clathrate would decompose into d-Si. A key question is whether such high temperatures are required with clathrates, or whether the metastable structure allows damage to be repaired and localized atomic motion to occur at lower temperatures. Implantation was performed at varying fluences and energies allowing for an examination of the clathrate's response to the implantation and activation process and possible damage recovery methods. These experiments also shed light on the interplay between implantation parameters and material properties, such as phase stability and amorphization of the Si clathrate to amorphous silicon (a-Si).

Methods

Silicon clathrate films were synthesized through a multistep decomposition procedure. To prepare for synthesis, a tantalum crucible (99.95% purity) detailed in ref. 20, was loaded into a 1.25 inch outer diameter quartz tube. A stainless-steel endcap was attached to the open end of the quartz tube with an o-ring attachment. This endcap allows the tube to be connected to flowing Ar or placed under vacuum, which is detailed further in ref. 23. This set up allows for isolation from the atmosphere during transportation between an argon filled glove box (<1 ppm O_2 and 0 ppm H_2O) and a 1100C MTI tube furnace. The Ta crucible was annealed at 500 °C for 30 minutes inside the set up under argon to remove any moisture or oxygen trapped in the crucible. The set up was then moved into the argon-filled glovebox and the crucible was loaded with ~10 mg of Na metal (99% purity, Sigma-Aldrich) that had previously been cleaned by melting at 400 °C, and impurities removed from the surface, and then spread on the bottom of the crucible. A 12×25 mm^2 n-type, Czochralski-grown, phosphorous (10–20 Ω cm) doped ⟨100⟩ Si wafer (WaferPro) that had been washed with methanol, deionized water (DI), and acetone was placed polished side down on a lip on the wall of the crucible about 5 mm above the Na metal. The lid of the crucible was then placed above the Si wafer and the crucible was wrapped in 99% pure aluminum foil.

For the silicide forming step, the wrapped crucible was loaded back into a quartz tube and the endcap was reattached and the set up was moved out of the glove box to the tube furnace. The furnace was ramped at 5 °C per minute to 550 °C

and held for 70 minutes with the set up under flowing argon. The furnace was allowed to cool to room temperature and then the set up was moved back into the glovebox. The procedure formed a Na_4Si_4 film on the surface of the Si substrate. For the decomposition step, the Na_4Si_4 film on Si substrate was then removed from the crucible and placed face up alone in a cleaned quartz tube.

The set up was then placed back in the furnace and heated to 400 °C in 10 min and held for 24 hours under dynamic vacuum (1×10^{-6} Torr) to decompose the Na_4Si_4 into Na_xSi_{136}. For the last step, to drive out excess Na, the furnace was immediately ramped to 430 °C at 1 °C per min and held for 48 hours. The furnace was then allowed to cool to room temperature and then the film was removed and washed in ethyl alcohol and rinsed in DI water and blown dry.

Prior work has shown this growth process can result in an amorphous layer and residual Na dense regions on the surface and grain boundaries of the resulting clathrate film.[11] To remove this the samples were reactive ion etched in SF_6 for 2.5–3 min with a microwave power of 250 W at 13.56 MHz under a pressure of 0.4 Torr. The resulting films were ~8 μm thick determined using a KLA Tencor D-600 stylus profilometer. Images of the Na_xSi_{136} grown on a Si substrate are shown in Fig. S1.

Stopping and range of ions in matter (SRIM) calculations were performed using the SRIM online toolbox, and shown in Fig. S2.[45] Diamond Si was used as a surrogate for the clathrate since Si clathrate parameters are not yet known. This was performed for both Li and Mg implant species to determine effective implant fluences and energies and understand depth profiles. The films then underwent either FIB implantation or BB implantation. For FIB implantation, in order to identify implanted regions, gold with a Cr adhesion layer was deposited onto the sample surface through a 50 μm thick steel shadow mask creating a 17 mm^2 square grid that was used as reference marks for implantation and subsequent characterization. The layout of this mask and an SEM image of a patterned sample are shown in Fig. S1. Mg and Li ion sources detailed further in ref. 46 and 47 were used to implant 150×150 μm^2 and 25×25 μm^2 regions respectively, on the Nano Implanter at Sandia National Laboratories. Implants were performed for Li with energies and fluences from 10 to 35 keV and from 10^{13} to 10^{15} ions cm^{-2}, respectively, with beam currents ranging from 0.24 to 1.06 pA. For Mg, energies of 10–60 keV and fluences from 10^{13} to 10^{15} ions cm^{-2} were used with beam currents of 102–165 pA. Lower beam current implants of 28.8–49.2 pA were also performed at 10, 20, 40, and 60 keV for all fluences. A schematic of the FIB implantation and characterization is shown in Fig. 1.

For BB implantation at Los Alamos National Laboratory, 5×5 mm^2 samples underwent Mg implantation in a 200 kV Danfysik research ion implanter ranging in energies from 30 to 50 keV and fluences of 1×10^{14}–7×10^{15} ions cm^{-2}, the maximum fluence achievable by the equipment, across the entire sample surface. The implantations performed are summarized in Table S1. In general, removal of implantation damage and activation of implanted dopants in semiconductors is accomplished through a post implant thermal annealing step. To study the effect of thermal annealing on the implants prepared here, a ULVAC-RIKO MILA-5000 mini lamp annealer

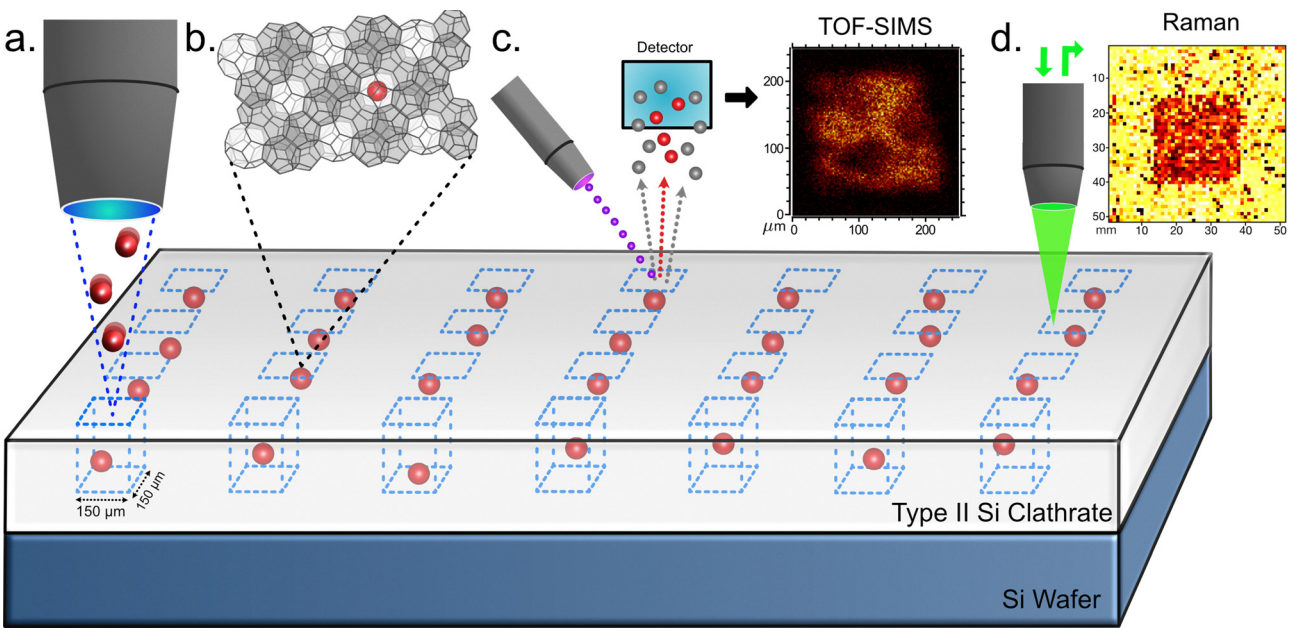

Fig. 1 Focused ion beam implantation of type II Si clathrate film (gray) on d-Si substrate (blue) and characterization. (a) The Si clathrate films were implanted with Mg ions (red) in 150×150 μm^2 regions varying the fluence, implant energy, and current across the Si clathrate film represented by the Mg being at different locations and depths in the blue implant regions. (b) The clathrate cage structure is shown in gray with darker shaded small cages, and a representative Mg ion in a lighter large cage. After implantation the films were characterized to assess implant, damage introduced, and stability of the clathrate material. (c) and (d) A spatially resolved TOF-SIMS ion image and confocal Raman map.

was used for rapid thermal annealing (RTA) between 300 and 700 °C under flowing argon.

The films were characterized before and after implantation, as well as after annealing, using multiple techniques. Ion images and intensities were acquired using an IONTOF TOF.-SIMS 5 time-of-flight secondary ion mass spectrometer, equipped with a 30 keV Bi^+ primary ion beam from a three-lens BiMn cluster ion gun, and an O_2 sputter beam from an oxygen electron impact gas ion source. Raman spectroscopy was performed using a WiTec Alpha 300 confocal Raman microscope equipped with a 532 nm laser, which has a 1 μm probing spot. XRD measurements were performed utilizing either a D500 Siemens X-ray diffractometer using the Cu Kα line of a Cu anode radiation tube (voltage 35 kV, current 30 mA) or a Panalytical Empyrean X-ray diffractometer for microbeam measurements with a Cu source (voltage 45 kV, current 40 mA). Scanning electron microscopy (SEM) was performed utilizing a TESCAN S8252G ultrahigh resolution variable pressure Schottky field emission scanning electron microscope. Spin density EPR measurements were performed in a X-band Bruker EMX EPR system equipped with a Bruker ColdEdge closed cycle He cryostat with a base temperature of ~4.2 K and modeled utilizing EasySpin.[48] For these measurements the clathrate film was removed from the Si substrate and flame sealed under vacuum in a quartz EPR tube. EPR analysis, as detailed in ref. 49, was used to determine Na content before implantation and indicated near guest free Si clathrate ($x \ll 1$), with a total Na concentration on the order of 10^{18} cm^{-3} as the starting material.

Results

Focused ion beam implantation

Ion implantation of conventional semiconductors, like d-Si, creates lattice damage which is typically repaired with post implant annealing. At sufficiently high energies and fluences, however, this damage can be unrecoverable leading to amorphous material.[50,51] The metastability of type II Si clathrate creates an additional consideration with the possibility that damage can catalyze conversion back to d-Si. In unimplanted materials this conversion does not occur until it is exposed to temperatures in excess of ~480–520 °C.[20,52] The first aim of the study was to identify thresholds in implantation parameters where the metastable Si clathrate material is converted into a-Si or d-Si. To determine this threshold, systematic FIB implantation experiments were conducted targeting small regions of near guest free Na_xSi_{136} film, approximately 150 × 150 μm^2 in size. Before and after implantation these films went through TOF-SIMS, SEM, and Raman analysis to determine the impact of the implantation on the clathrate film.

Critical to the FIB study was the ability to locate the relatively small implanted regions during characterization measurements. Accomplishing this took advantage of the metal reference grid deposited on the sample. A coordinate system using the corners of the grid as starting locations was used to locate implanted regions. Each implant series began with the highest

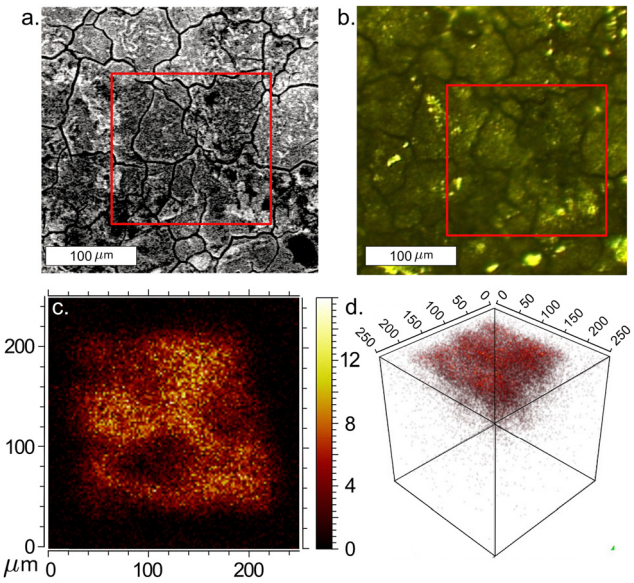

Fig. 2 (a) SEM image of Mg implantation into a Na_xSi_{136} film with high fluence (10^{15} ions cm^{-2}) outlined in red. (b) Raman confocal microscope image of the same area with the red box indicating grains used for matching locations for large area scans. (c) and (d) TOF-SIMS Mg intensity profile 2D and 3D image of the Mg implants.

fluence. The sample was then moved 100 μm in the direction of one of the grid lines for each subsequent implant. This system could be validated by the fact that at the highest fluence (10^{15} ions cm^{-2}) and higher energy (30 keV and above) the implanted regions were clearly visible in SEM images (Fig. 2(a)), where the implant can be seen as the darker region highlighted inside the red box. A portion of the next lower fluence implant is visible as a dark region to the left. SEM was used to identify the first few implants in the series and to confirm the spacing and direction to subsequent implant regions. The grain structure of the film could then be matched to find the same regions in confocal Raman scattering, shown in Fig. 2(b). Often several of the square implant regions could then be identified directly in Raman as discussed below. While this approach worked quite well for Mg implantation it was never possible to detect Li implanted regions in our study. We begin by discussing the Mg implanted regions and then return to a discussion of difficulties detecting Li.

TOF-SIMS analysis of Mg implanted samples revealed distinct depth profiles for magnesium implantation, clearly indicating the incorporation of Mg into the type II Si clathrate film as shown in Fig. 2(c) and (d). TOF-SIMS measurements were taken at multiple Mg implant locations and were able to detect the square implant region and build 3D profiles of implant depth indicating the implants were localized very near the surface, within the top half micron of the film. These depth profiles were compared to the SRIM predictions shown in Fig. S2 that indicated an expected depth of ~400 nm or less consistent with the measured TOF-SIMS profiles.

The critical fluence, the fluence at which an implanted material becomes amorphous, has been heavily investigated

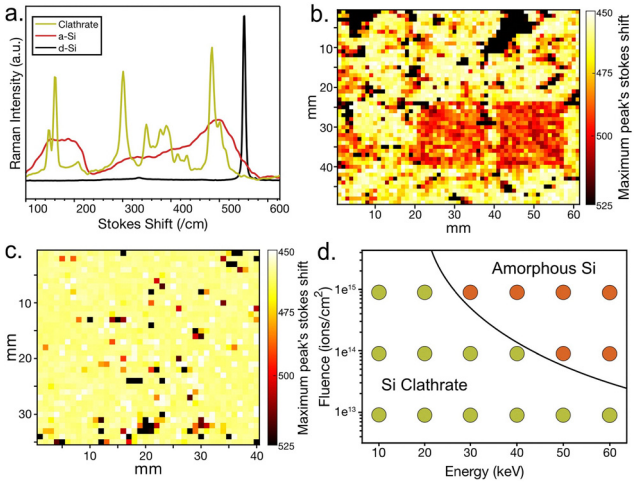

Fig. 3 (a) Raman spectra of Na_xSi_{136} in yellow, amorphous silicon in red, and diamond silicon in black. (b) Large area Raman scan of the 60 keV implants with the spectra filtered by maximum peak intensity between 450–530 cm^{-1} and identified as type II Si clathrate (yellow), a-Si (orange), or d-Si (black) showing clear damaged regions corresponding with a-Si at 10^{14} and 10^{15} ions cm^{-2} fluences. (c) Large area Raman scan of the 20 keV implants showing no damaged regions. (d) Summary of Raman spectrum Mg implantation into type II clathrate film. The orange circles indicate samples that showed conversion to a-Si in Raman area scans. The yellow circles indicate the Si clathrate structure was retained after implantation.

in many materials and in particular in d-Si.[53–55] In general, it depends on the mass and energy of the implanted species, as well as the implant temperature. As mass and energy increase, the critical fluence decreases, while increasing temperature increases critical fluence. This amorphous transformation is visible in confocal Raman scattering images of the Mg implanted regions. Raman spectra from type II Si clathrate, a-Si, and d-Si are quite different as shown in Fig. 3(a). The type II spectrum was collected from a film before implantation, the a-Si spectrum is from a highly amorphized region after implantation, and the d-Si spectrum is from the Si substrate with no film. In the 450–530 cm^{-1} region type II Si clathrate exhibits a dominant E_g symmetry peak around 466 cm^{-1}, a-Si has a broad feature around 480 cm^{-1}, and d-Si has a single peak at 521 cm^{-1}.

The implanted regions were mapped using the confocal Raman microscope to acquire Raman spectra while scanning the acquisition point across sample regions. The spectra were then filtered by looking for the maximum intensity between 450–530 cm^{-1} allowing each location's composition to be identified as type II Si clathrate, a-Si, or d-Si. It should be noted that no type I Si clathrate peaks were identified in Raman before or after implantation. A large area Raman map was then created for each of the implant regions. Spectra were acquired every 10 μm with the value assigned to each pixel in Fig. 3(b) and (c) representing the Raman shift of the maximum peak of the Raman spectrum acquired at that location. The mapping of the 60 keV implants is shown in Fig. 3(b) with the amorphized 150 × 150 μm^2 region of the 10^{14} and 10^{15} ions cm^{-2} fluence implants clearly visible while the 10^{13} ions cm^{-2} fluence implant directly to the left of the 10^{14} ions cm^{-2} implant did not show conversion. The implant region of the 20 keV spot is shown in Fig. 3(c) with no clear implant regions visible, only some a-Si and d-Si appearing due to some locations being out of focus and sampling noise. These higher shift peaks could also be due to some inhomogeneity, damaged film, or sampling a grain boundary. This Raman mapping was performed at each of the implant locations. This established a trend that the 50 keV and above implants with fluence of 10^{14}–10^{15} ions cm^{-2} converted the surface material to a-Si. At 30–40 keV just the 10^{15} ions cm^{-2} fluence implants converted. All 10^{13} ions cm^{-2} fluence implants did not convert the material. In addition, the implants at lower beam currents, even at 60 keV, did not convert the material. The surface changes have been summarized in Fig. 3(d) and the black line has been added as a guide to the readers for the critical fluence threshold for these energies at room temperature. While there have not been studies of Mg implants at these energies in d-Si, studies of elements with similar masses show critical fluences, in-line with what is being observed.[53] Fig. 3(d) can be used to select parameters for subsequent BB implantation of larger area samples.

The critical fluence changes significantly in d-Si for lighter ions like Li.[53] Generally, the lighter the ion the higher the fluence threshold. This may be a reason why no amorphization was detected for any Li implants. Reported critical fluences for Li in d-Si are about five times higher than that of Mg at similar energies to those used in this study.[53] This is likely why no amorphization was detected from any Li implants. It is surprising that TOF-SIMS did not reveal higher Li content in the region associated with the implants. We note that Li is a fast diffuser, and it is possible that the implanted Li dispersed from the surface and reached levels not detectable above background in TOF-SIMS.

These results established an initial framework for understanding the localized effects of ion implantation, highlighting the influence of implantation energy and fluence on the extent of structural disruption. In the case of d-Si, for fluences below the critical fluence, damage can be repaired thermally as the implant is activated. Implants above the critical fluence are often used, but in this case the implanted material has to be heated sufficiently to recrystallize to d-Si. For metastable Si clathrate, recrystallization will undoubtedly result in d-Si, hence it is key to stay below the critical fluence and find ways of thermally repairing damage without recrystallization.

Thermal stability

Since dopant implants are generally activated thermally there is a need to examine what temperatures the clathrate material can withstand before converting back to d-Si. From previous work, it is known that the metastable Si clathrate material is stable up to ~470 °C but long exposures above this temperature can lead to degradation to d-Si.[20,52] Typical implant annealing in Si utilizes RTA to temperatures well above this and near 1200 °C.[44] However, in d-Si implants, typically the bonds need to be broken and reformed to activate the implant by moving it into a vacancy site to be a substitutional dopant in the lattice.

This can be done by the implant knocking a Si atom out of place and annealing to repair broken bonds, diffusing in vacancies, or by bonds breaking and reforming during the anneal. The goal of clathrate implants though, is to allow the implant dopant to diffuse into the Si clathrate cage through the rings without the need to break any bonds. Achieving this migration of the dopant should be easier than in d-Si due to the Si clathrate's large interstitial sites and with the dopant being in the cage instead of the framework, so the required temperatures may be lowered. Dopants like Na and Li have been shown to move in and out of cages at much lower temperatures around 300–400 °C.[20,24]

To understand the thermal stability of the clathrate structure, annealing studies were performed on low Na ($x \ll 1$) unimplanted Na_xSi_{136} film samples across a temperature range of 300 °C to 700 °C. The samples were ramped to the desired temperature in 12 s, held for 12 s, and cooled back to room temperature under flowing argon. XRD measurements confirmed the type II Si clathrate structure remained intact up to 475 °C. Above this temperature some d-Si conversion occurred indicated by the appearance of peaks forming at 28, 47, and 55 2θ shown in orange in the reference lines at the bottom of Fig. 4. This was believed to be due to a slow cooling rate after reaching the annealing temperature. It took around 10 min for the RTA chamber to return to room temperature. To test this, after heating to 500 °C, the sample was removed from the RTA quickly and cooled in air. This allowed for much shorter cooling times and as can be seen in the red patterns in Fig. 4, there was no evidence of d-Si in XRD following the 500 °C annealing step and only slight conversion at 600 °C with strong conversion at 700 °C. It should be noted that immediately quenching the clathrate film in DI water did not improve the stability beyond air cooling. Due to this, an annealing temperature of 500 °C with rapid cooling in air was chosen for the implant activation to allow for the highest activation temperature without the risk of converting any material to d-Si. Since this is a temperature close to where the Si clathrate converts to d-Si, it is also a temperature where bonds are mobile and reforming with the potential for repairing implantation damage. This behavior underscores the need for precise thermal management when processing Si clathrates, as their stability range is significantly lower than that of d-Si.

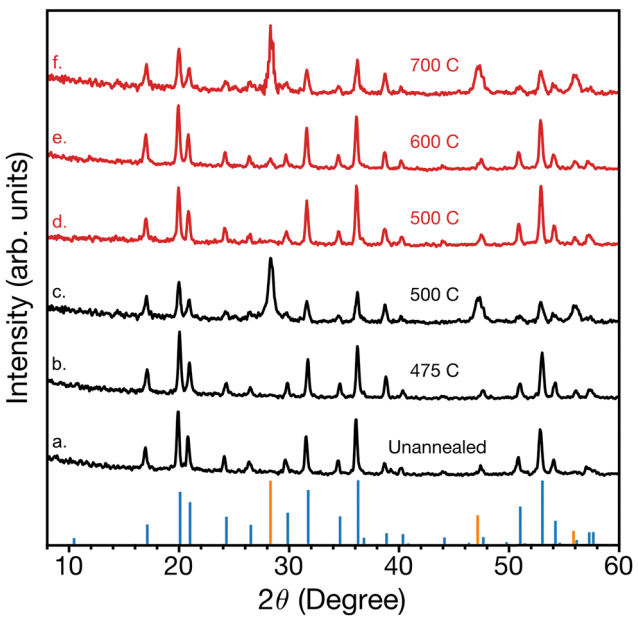

Fig. 4 XRD patterns Na_xSi_{136} film that were annealed at different conditions. The blue and orange lines represent the reference peaks of type II Si clathrate (ICDD 98-024-8181) and diamond silicon respectively. (a) Unannealed sample, (b) and (c) annealed in RTA and allowed to cool to room temperature under flowing argon, and (d)–(f) annealed in RTA and removed from annealer immediately and allowed to cool to room temperature in the atmosphere.

Broad ion beam implantation

After determining the critical fluence thresholds using FIB implantation, BB Mg-ion implantation was studied structurally using XRD and then electronically using EPR. An additional goal of the BB implantation experiments was to look for evidence of damage repair and implant activation after RTA. Broad beam Mg implant energies and fluences were chosen above and below critical fluence thresholds to examine this difference. The films were first characterized using TOF-SIMS and Raman spectroscopy to examine consistency with FIB implanted samples, showing overall good agreement.

TOF-SIMS analysis results, shown in Fig. 5(a), show implant profiles for the BB implanted Mg samples. The Mg signal was point-by-point normalized to the total ion yield (TIY) to correct for local ionization efficiency and primary beam current variation. As the implant fluence was increased the amount of Mg incorporated into the sample increased as expected. The sputter time was calibrated to depth by scanning the craters left by the TOF-SIMS milling using a profilometer and shown in Fig. S3. The integrated Mg counts for each implant is shown in the left inset. The integrated counts were found by summing the normalized counts within the top micron of each implant profile and dividing by the sputter area, 300×300 μm^2, followed by background subtraction of the unimplanted region. The top micron, shown in the right inset in Fig. 5(a), was used because most of the implanted Mg resides there, similar to SRIM predictions. The low intensity remainder of the profile is less reliable and may be caused by straggle and largely influenced by film roughness causing uneven sputtering rate across the sputter region. The exponent in this log–log plot is close to one indicating a linear dependence of Mg counts from TOF-SIMS and Mg fluence as expected and seen in the left inset.

XRD scans, shown in Fig. 5(b), of the BB Mg implants showed that there was no presence of additional phases even for the strongest of implant energy and fluences of 7×10^{15} ions cm^{-2} at 50 keV which was the highest fluence possible at this energy with the BB implanter. The higher implant energy films did show broadening of the XRD lines indicating potential lattice damage from the implantation process. The fluence is above the critical threshold in Fig. 3(d) and Raman does show the presence of amorphous material. Noticeably the

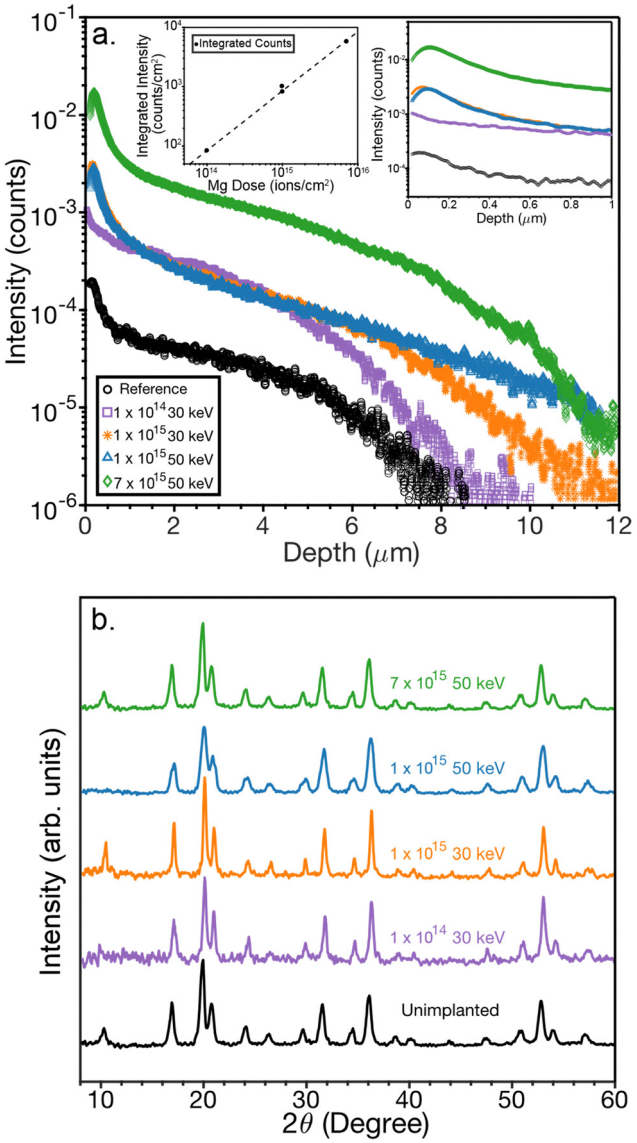

Fig. 5 (a) TOF-SIMS of broad beam implanted Na_xSi_{136} film samples. The right inset shows the first micron and left inset shows the integrated intensity as a function of fluence. (b) XRD of broad beam Mg implants of a Na_xSi_{136} film sample. The unimplanted sample is shown in black. As implant energy and fluence increases there is no noticeable change in phase to type I clathrate, a-Si, or d-Si.

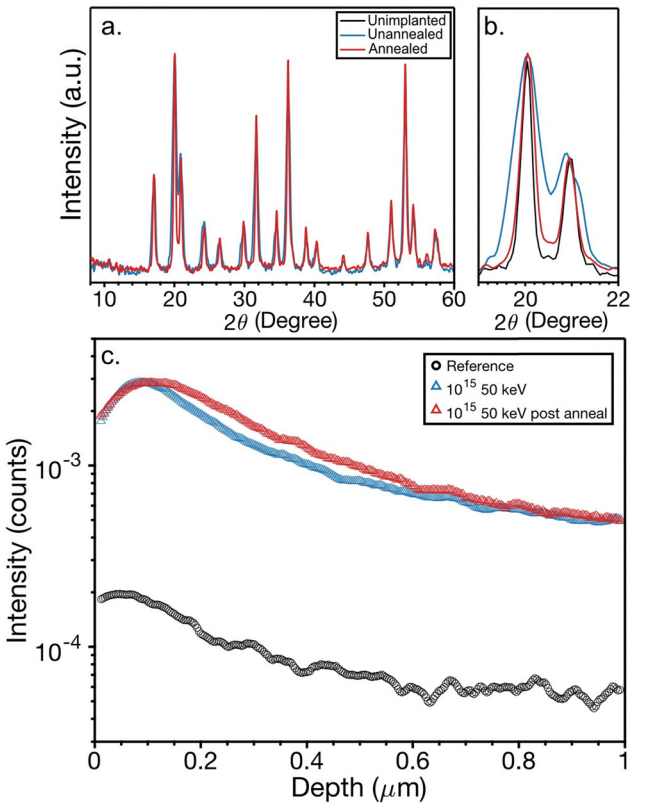

Fig. 6 (a) XRD of the pre (blue) and post (red) annealed 10^{15} ions cm^{-2} fluence at the 50 keV implanted sample. The broadening observed after implantation is reduced after annealing indicating a restoration in crystal structure. (b) XRD of the prominent peaks around 20 2θ to highlight the change in line width compared to the unimplanted original clathrate film (black). (c) TOF-SIMS of BB Mg implanted 10^{15} ions cm^{-2} fluence at 50 keV of the Na_xSi_{136} film sample. The black curve denotes the unimplanted sample for reference, blue is before annealing and red is post annealing.

XRD does not indicate a-Si typically seen as a broad background with a peak spanning ~20–35 2θ in Si clathrate XRD.[11] This suggests the damage to the Si clathrate film from the implantation process is very shallow with Raman and XRD sampling different depths. The effective sampling depth of the XRD is around ~7–9 μm at these diffraction angles, based on a low Na content Si clathrate density of 2.017 g cm^{-3} giving a mass attenuation coefficient, μ = 123.2.[56] The Raman sampling space is much more sensitive to the implanted region. The clathrate absorption coefficient, α, at the 532 nm wavelength of the Raman laser, is ~4×10^4 cm^{-1} corresponding to a measurement depth of 0.25 μm.[11] The fraction of a-Si would need to be much more substantial to be seen in the XRD pattern. This indicates that the amorphous material is near the surface and detectable by Raman, but not by XRD which samples the entire film.

Rapid thermal annealing was then performed on the BB Mg implanted films at 500 °C for 12 seconds and the films were recharacterized in XRD, Raman, and TOF-SIMS. Fig. 6(a) shows the XRD pattern of the 1×10^{15} ions cm^{-2} fluence at 50 keV implant energy. After annealing the film continues to show a crystalline clathrate pattern, but the line broadening that was observed after implantation is noticeably reduced, highlighted in Fig. 6(b) for the peaks located at 20 and 21 2θ. This reduction in broadening, close to the unimplanted pattern in black, may indicate a reduction in the lattice defects and more crystalline Si clathrate material.

The TOF-SIMS profile after annealing showed a redistribution of the Mg which diffused further into the film, similar to annealing profiles of Mg in d-Si.[57] This is shown in Fig. 6(c) by the shift of the peak to the right in the annealed film. The integrated intensity did not decrease after annealing showing the Mg was not driven back out due to the annealing process. Complexes like Mg–Si and Mg–Na were also looked for in TOF-SIMS. While these species appeared in the mass spectrum, no

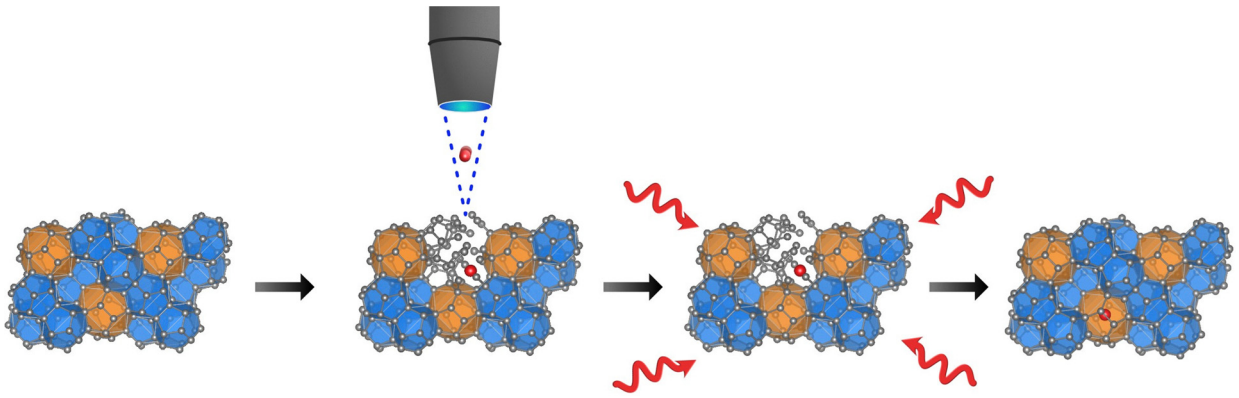

Fig. 7 Ion implantation of type II Si clathrate with large (orange) and small (blue) cages and implanted ion (red).

significant differences were observed in their intensities before implantation, after implantation, or after annealing. They are therefore considered background, likely arising from impurities in the films or residual species from previous samples run in the system. The plots of each can be seen in Fig. S4. Mg–Mg dimers were also examined and were similarly seen in the mass spectrum but have mass overlap with SiF complexes known to be on the film surface after SF_6 etches and did no show increases after implantation or annealing. A schematic of the annealing process and potential recovery and implant diffusion is shown in Fig. 7. In the left-most panel the low Na type II Si clathrate films start relatively guest free with empty small and large cages. In the next panel after implantation the implant likely bumps and knocks some atoms slightly out of place before stopping, leading to the broadening seen in Fig. 5 and 6 from the XRD analysis. The third panel shows the implant activation taking place using RTA. Finally in the right-most panel the implanted ion drives slightly deeper into a cage with atoms repositioning and bonds repairing themselves.

Raman still exhibited an amorphous spectrum and did not show any significant changes before and after annealing of the higher energy high dose implants. Raman spectra of lower energy 30 keV implants with 1×10^{15} ions cm^{-2} also remained largely indicative of a-Si. However, large area scans sampling many positions showed the consistent reemergence of type II Si clathrate peaks across the sample. The type II Si clathrate Raman peaks were maintained for the 30 keV 1×10^{14} ions cm^{-2} sample (which is below the critical fluence) before and after annealing, as shown in Fig. S5.

The EPR spectra of the Si clathrate samples were also characterized before Mg implantation and after Mg implantation and activation. Here we focus on several EPR features that have been identified in prior studies and assigned to spin active species in Na doped type II Si clathrate films.[23,49,58,59] The films were examined across a wide temperature range from room temperature to 5 K. The room temperature EPR spectra before implantation (black) and after implantation and activation (red) are shown in Fig. 8(a). In modulation CW-EPR the derivative of the absorption spectrum is observed. The large feature present in both room temperature spectra is associated with an absorption peak arising from unterminated silicon bonds (dangling bonds) with unpaired electrons contributing to the EPR signal at a g value of $\sim$2.005. The other significant room temperature feature, which only appears in the Mg implanted and annealed sample, is a smaller bump superimposed on the center of the dangling bond feature. This is associated with conducting electrons or free carriers in the sample with a g value of $\sim$2.003, close to that of a free electron of 2.0028. These features are consistent with other EPR analysis of these materials.[49] This difference in the spectra is also noticeable in the absorption spectra obtained from integrating the EPR signal, shown in the inset of Fig. 8(a). The additional free carrier feature causes a shift of the absorption peak to the right. These spectra can be fit following procedures detailed further in ref. 49 to determine the increase in free carriers. The free carrier concentration increased by around $\sim 2 \times 10^{15}$ cm^{-3}. This corresponds to $\sim 4 \times 10^{11}$ spins when multiplied by the sample volume. The 5×5 mm^2 10^{15} cm^{-2} fluence implant is $\sim 3 \times 10^{10}$ spins. The free carrier peak has been shown to increase with subsequent annealing in previous work due to redistribution of atoms which could account for this increase.[20] Additional measurements were performed on unimplanted type II Na_xSi_{136} before and after annealing following the same procedures as the implanted samples and indicated a free carrier increase shown in Fig. S6(a). This suggests the increase is not entirely due to the implant, but rather from the annealing causing repair of residual defects or better activation of the Na in the starting material.

At low temperature, the EPR spectrum of the unimplanted sample, shown in black in Fig. 8(b), is typical of low Na type II Si clathrate. Here we focus on the four hyperfine lines associated with the donor electron interacting with the isolated spin 3/2 Na nucleus and the clustered Na feature centered at 330 mT, which is more easily seen in the integrated spectrum in the inset. Magnesium, with two valence electrons, is expected to be electronic spin zero and not directly detectable in low temperature EPR. Mg does have a naturally occurring (about 10.1%) nuclear spin 5/2 Mg^{25} isotope, but this low percentage of isotope along with the low doping makes it unlikely to see contributions from this species. The other isotopes Mg^{24} and

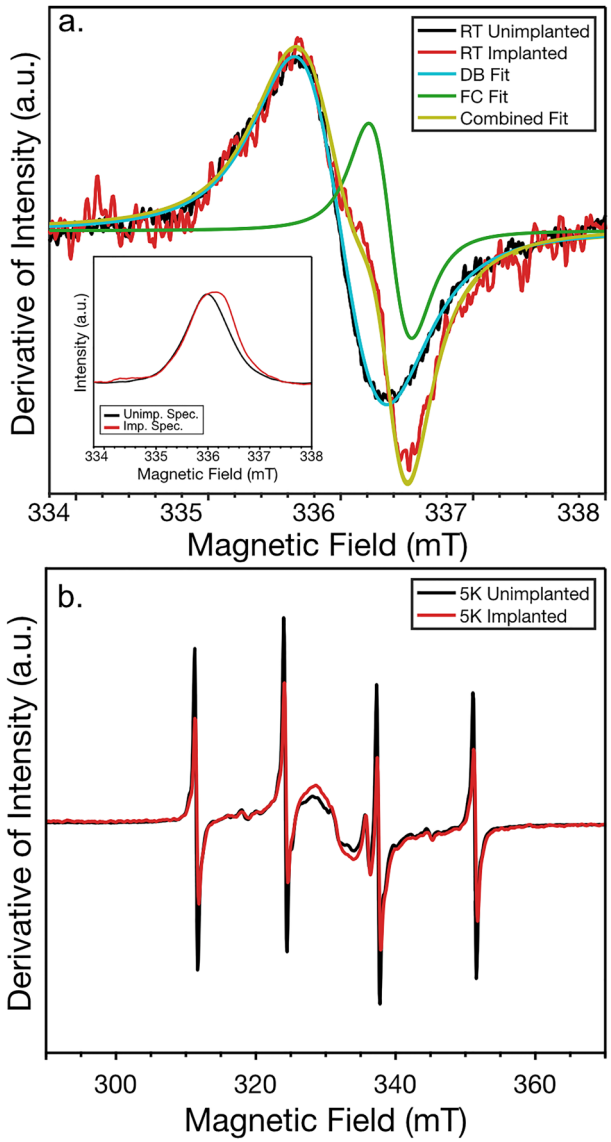

Fig. 8 (a) Room and (b) low (5 K) temperature CW-EPR of the Na_xSi_{136} film before implantation (black) and after 10^{15} ions cm^{-2} fluence implantation and annealing (red). The spectra were acquired under the same parameters at 9.44 GHz over 40 scans at room temperature and 10 scans at low temperature and scaled by sample weight. The insets showing the integrated absorption spectra.

Mg^{26}, which make up ~79% and 11% respectively, are nuclear spin zero.[60]

The presence of Mg was, however, detected indirectly through its effect on the Na hyperfine lines which decreased significantly in intensity after implantation and annealing as shown in Fig. 8(b). The low temperature EPR of the unimplanted annealed Si clathrate film sample, in Fig S6(b), showed an opposite strong increase in the hyperfine lines. This suggests that Mg is interacting with the Na donor electron decreasing the number of isolated Na atoms in the material. Similar suppression of hyperfine lines was observed when Li was incorporated into low Na type II Si clathrate. The suppression was attributed to Li and Na forming spin zero pairs.[20] In the present case given Mg has two valence electrons the nature of the interaction is less clear, but being able to attribute the decreased hyperfine lines with the implant of Mg suggests the Mg is in close proximity to the Na and does affect the electronic configuration of the Na.

For the broad Na cluster feature the situation is less clear. When Li was introduced both the isolated and cluster Na features decreased in intensity. In the present case, the isolated Na lines decrease but the cluster feature grows. This seems to indicate that there is less isolated Na and more Na in neighboring cages forming clusters after implantation of Mg and annealing. Although this could be due to local diffusion and rearrangement of Na atoms during implant and anneal stages, we think this is unlikely since changes like this are not observed in unimplanted samples subject to the same annealing treatment, shown in Fig. S6(b). In the unimplanted sample the hyperfine lines and the cluster feature increase from the thermal annealing process. While the cluster signal in the implanted samples increases, it is not to the extent of the annealed unimplanted sample, suggesting there could be some suppression of the cluster feature as well. It's possible there are two effects happening in the implanted sample, increase in the Na cluster feature due to defect repair and Na rearrangement after annealing, and suppression due to Mg interacting with the Na. Additionally, EPR spectra were taken at incremental temperatures from 5 to 150 K to attempt to see the possible thermalization of a single Mg electron, which would leave the Mg spin active, however, no additional features consistent with a spin from a single Mg donor electron were observed. The temperature dependent EPR is shown in Fig. S7. While we do not see the Mg directly in EPR and cannot be sure precisely where it sits, we are able to detect its presence and suspect it likely does move into the cages due to the way it is affecting the signatures of Na atoms already in the cages.

Conclusions

A key challenge with type II Si clathrate materials is the lack of synthesis methods that incorporate guests/dopants lying outside of the column one. In this work we showed that ion implantation into Si clathrate films is a functional and specific way to introduce alternative dopants in a highly controllable means. While the metastable Si clathrate material can convert to d-Si or amorphous phases, we have found, through examining a variety of implant fluences and energies, where it is possible to implant dopants into the films without these conversions. It is also possible to thermally anneal the implants in temperature ranges where the implanted ions move, indications of damage are reduced, and the metastable clathrate structure is maintained. It should be noted that a tradeoff between critical fluence and implant energy was found to be consistent with ion implantation studies of d-Si. This suggests that high fluence implants without amorphizing the material may be possible. In addition, the metastable nature of the Si clathrate material could have a potential advantage if damage

repair and dopant activation can occur at lower temperatures. In particular, dopants may be able to enter cages with low activation energy due to the ability to pass atoms through the open rings structure of the cage, without the need for breaking and reforming bonds or to create defects in the lattice.

This study opens the door for utilizing ion implantation as a means to implant specific dopant materials and at specific concentrations for device applications to enhance electrical, optical, thermal, and quantum properties. Although ion implantation of Mg into related materials like d-Si has been well studied and other approaches to incorporating Mg into d-Si, such as thermal diffusion, have been explored,[61–63] incorporation of Mg into Si clathrates by any method has never been demonstrated. In addition to our study's demonstration that ion implantation can be performed without conversion to d-Si, implantation also has advantages over methods like thermal diffusion, SPS, and HPHT in the precise control over where species are located in the film. Typical methods employ a more uniform distribution across the film surface and do not allow for spatial control over dopants, where ion implantation, as demonstrated in this study, can pinpoint specific areas of films to dope. Future research should aim to expand the range of dopants studied in Si clathrates, and explore elements beyond Mg that could further enhance their electronic, optical, and spintronic properties. Additionally, investigating the effects of doping with multiple species and the interactions between different dopants may provide new pathways for tuning these materials. This is a particular strength of ion implantation over other developed methods that function by forming the Si clathrate around a single dopant. Integration into devices is an important goal, which requires more control over doping than presently exists. For example, an effective p-type dopant has yet to be developed. Furthermore, FIB implantation in tandem with lithography and other semiconductor processing techniques could allow for the precision needed for advancements in Si allotrope-based devices to allow these materials to become players in the fields of CMOS and quantum dots. Preliminary work has been performed on using clathrates as a host material for spin-based qubits but noted a need for decreased doping levels and alternative guests,[23] both of which this method could provide. Ion implantation could be an important aspect, of a route not possible under other methods, to device applications that takes advantage of these exciting materials.

Author contributions

J. P. B.: conceptualization, data curation, formal analysis, investigation, methodology, visualization, writing – original draft, reviewing & editing. S. S.: investigation, methodology. M. W.: investigation, formal analysis. S. S. S.: investigation, methodology. M. T.: investigation, methodology, resources, writing – reviewing & editing. Y. W.: investigation, methodology, resources, writing reviewing & editing. Y. L.: investigation, methodology. R. T. C.: conceptualization, formal analysis, methodology, resources, supervision, writing – reviewing & editing. M. S.: conceptualization, funding acquisition, methodology, project administration, resources, supervision, writing – reviewing & editing. C. A. K.: conceptualization, data curation, funding acquisition, project administration, resources, supervision, writing – reviewing & editing.

Conflicts of interest

There are no conflicts to declare.

Data availability

Data for this article, including XRD, EPR, Raman, and TOF-SIMS measurements are available at Mines Repository at **https://doi.org/10.25676/11124/180801**.

The SI includes further information on sample preparation and implanation procedures, SRIM, TOF-SIMS depth profiling and additional species, Raman of annealend and unannealed samples, EPR of annealed samples, and the temperature dependant EPR. See DOI: **https://doi.org/10.1039/d5ma00603a**.

Acknowledgements

This work was supported by the National Science Foundation, Grant No. 2114569 (clathrate synthesis and characterization, JPB and SS) and the Center for Integrated Nanotechnologies (CINT), proposal No. 2022BU0159 (implantation), jointly operated by Los Alamos and Sandia National Laboratories. This work was performed, in part, at the CINT, an Office of Science User Facility operated for the U.S. Department of Energy (DOE) Office of Science. Sandia National Laboratories is a multimission laboratory managed and operated by National Technology and Engineering Solutions of Sandia, LLC, a wholly owned subsidiary of Honeywell International, Inc., for the U.S. DOE's National Nuclear Security Administration (NNSA) under contract DE-NA-0003525. Los Alamos National Laboratory, an affirmative action equal opportunity employer, is managed by Triad National Security, LLC for the U.S. Department of Energy's NNSA, under contract 89233218CNA000001. This material makes use of the TOF-SIMS system at the Colorado School of Mines, which was supported by the National Science Foundation under Grant No. 1726898. The authors would also like to acknowledge Sara Russo for her help with training on the Tescan instrumentation.

References

1 J. S. Kasper, P. Hagenmuller, M. Pouchard and C. Cros, *Science*, 1965, **150**, 1713.
2 C. Cros, M. Pouchard and P. Hagenmuller, *J. Solid State Chem.*, 1970, **2**, 570.
3 Y. Liu, J. P. Briggs, R. T. Collins, M. Singh, P. C. Taylor and C. A. Koh, *Appl. Phys. Lett.*, 2025, **126**, 090501.

4 J. Slingsby, N. Rorrer, L. Krishna, E. Toberer, C. Koh and C. Maupin, *Phys. Chem. Chem. Phys.*, 2016, **18**, 5121.
5 G. Nolas, J. Cohn, G. Slack and S. Schujman, *Appl. Phys. Lett.*, 1998, **73**, 178.
6 J.-A. Dolyniuk, B. Owens-Baird, J. Wang, J. V. Zaikina and K. Kovnir, *Mater. Sci. Eng., R*, 2016, **108**, 1.
7 G. Nolas, M. Beekman, J. Gryko, G. Lamberton Jr, T. Tritt and P. McMillan, *Appl. Phys. Lett.*, 2003, **82**, 910.
8 M. Beekman and G. Nolas, *Phys. B*, 2006, **383**, 111.
9 M. Beekman, K. Wei and G. S. Nolas, *Appl. Phys. Rev.*, 2016, **3**, 040804.
10 A. K. Bharwal, R. Vollondat, C. Tamin, S. Roques, J. Bartringer, D. Stoeffler, C. Chevalier, A. Dinia, A. Slaoui and T. Fix, *ACS Appl. Energy Mater.*, 2024, **7**, 8554.
11 Y. Liu, W. K. Schenken, L. Krishna, A. A. Majid, T. E. Furtak, M. Walker, C. A. Koh, P. C. Taylor and R. T. Collins, *Appl. Phys. Rev.*, 2021, **8**, 041408.
12 T. Fix, R. Vollondat, A. Ameur, S. Roques, J.-L. Rehspringer, C. Chevalier, D. Muller and A. Slaoui, *J. Phys. Chem. C*, 2020, **124**, 14972.
13 L. L. Baranowski, L. Krishna, A. D. Martinez, T. Raharjo, V. Stevanović, A. C. Tamboli and E. S. Toberer, *J. Mater. Chem. C*, 2014, **2**, 3231.
14 A. K. Bharwal, J. P. Briggs, C. Tamin, M. Hanauer, R. Vollondat, J. Bartringer, S. Roques, C. Chevalier, A. Dinia and R. T. Collins, *et al.*, *ACS Appl. Energy Mater.*, 2025, **8**, 1752.
15 A. K. Bharwal, J. P. Briggs, C. Tamin, M. Hanauer, M. Lenertz, J. Bartringer, S. Roques, C. Chevalier, M. Gallart and P. Gilliot, *et al.*, *Phys. Status Solidi RRL*, 2025, e202500318.
16 L. Krishna, A. D. Martinez, L. L. Baranowski, N. P. Brawand, C. A. Koh, V. Stevanović, M. T. Lusk, E. S. Toberer and A. C. Tamboli, *Physics, Simulation, and Photonic Engineering of Photovoltaic Devices III*, 2014, vol. 8981, p. 29.
17 A. D. Martinez, L. Krishna, L. L. Baranowski, M. T. Lusk, E. S. Toberer and A. C. Tamboli, *IEEE J. Photovolt.*, 2013, **3**, 1305.
18 P. Warrier and C. A. Koh, *Appl. Phys. Rev.*, 2016, **3**, 040805.
19 A. Dopilka, A. Childs, S. Bobev and C. K. Chan, *J. Electrochem. Soc.*, 2021, **168**, 020516.
20 Y. Liu, J. P. Briggs, A. A. Majid, T. E. Furtak, M. Walker, M. Singh, C. A. Koh, P. C. Taylor and R. T. Collins, *Inorg. Chem.*, 2023, **62**, 6882.
21 S. Yamanaka, E. Enishi, H. Fukuoka and M. Yasukawa, *Inorg. Chem.*, 2000, **39**, 56.
22 J.-M. Hübner, Y. Prots, W. Schnelle, M. Bobnar, M. König, M. Baitinger, P. Simon, W. Carrillo-Cabrera, A. Ormeci and E. Svanidze, *et al.*, *Chem. – Eur. J.*, 2020, **26**, 830.
23 J. P. Briggs, Y. Liu, P. C. Taylor, M. Singh, R. T. Collins and C. A. Koh, *Appl. Phys. Lett.*, 2024, **125**, 202402.
24 L. Krishna, L. L. Baranowski, A. D. Martinez, C. A. Koh, P. C. Taylor, A. C. Tamboli and E. S. Toberer, *CrystEngComm*, 2014, **16**, 3940.
25 G. K. Ramachandran, P. F. McMillan, J. Dong and O. F. Sankey, *J. Solid State Chem.*, 2000, **154**, 626.
26 W. D. Gunatilleke, O. P. Ojo, H. Poddig and G. S. Nolas, *J. Solid State Chem.*, 2022, **311**, 123152.
27 E. Reny, S. Yamanaka, C. Cros and M. Pouchard, *Chem. Commun.*, 2000, 2505.
28 I. Veremchuk, M. Beekman, I. Antonyshyn, W. Schnelle, M. Baitinger, G. S. Nolas and Y. Grin, *Materials*, 2016, **9**, 593.
29 N. Mott, *J. Solid State Chem.*, 1973, **6**, 348.
30 S. Roy, K. Sim and A. Caplin, *Philos. Mag. B*, 1992, **65**, 1445.
31 J. Williams, *Mater. Sci. Eng., A*, 1998, **253**, 8.
32 K. S. Jones, S. Prussin and E. Weber, *Appl. Phys. A: Solids Surf.*, 1988, **45**, 1.
33 M. I. Current, *Mater. Sci. Semicond. Process.*, 2017, **62**, 13.
34 P. Li, S. Chen, H. Dai, Z. Yang, Z. Chen, Y. Wang, Y. Chen, W. Peng, W. Shan and H. Duan, *Nanoscale*, 2021, **13**, 1529.
35 L. V. Goncharova and P. J. Simpson, *Physics*, 2022, **4**, 383.
36 K. Gamo, *Mater. Sci. Eng., B*, 1991, **9**, 307.
37 V. Chandrasekaran, M. Titze, A. R. Flores, D. Campbell, J. Henshaw, A. C. Jones, E. S. Bielejec and H. Htoon, *Adv. Sci.*, 2023, **10**, 2300190.
38 N. Delegan, S. J. Whiteley, T. Zhou, S. L. Bayliss, M. Titze, E. Bielejec, M. V. Holt, D. D. Awschalom and F. J. Heremans, *Nanotechnology*, 2023, **34**, 385001.
39 M. Titze, H. Byeon, A. Flores, J. Henshaw, C. T. Harris, A. M. Mounce and E. S. Bielejec, *Nano Lett.*, 2022, **22**, 3212.
40 D. N. Jamieson, S. Prawer, I. Andrienko, D. A. Brett and V. Millar, *Nucl. Instrum. Methods Phys. Res., Sect. B*, 2001, **175**, 744.
41 S. Moffatt, P. Hemment, S. Whelan and D. Armour, *Mater. Sci. Semicond. Process.*, 2000, **3**, 291.
42 D. Holmes, B. Wilhelm, A. M. Jakob, X. Yu, F. E. Hudson, K. M. Itoh, A. S. Dzurak, D. N. Jamieson and A. Morello, *Adv. Quantum Technol.*, 2024, **7**, 2300316.
43 T. Schröder, M. E. Trusheim, M. Walsh, L. Li, J. Zheng, M. Schukraft, A. Sipahigil, R. E. Evans, D. D. Sukachev and C. T. Nguyen, *et al.*, *Nat. Commun.*, 2017, **8**, 15376.
44 R. Chow and R. Powell, *J. Vac. Sci. Technol., A*, 1985, **3**, 892.
45 J. F. Ziegler, M. D. Ziegler and J. P. Biersack, *Nucl. Instrum. Methods Phys. Res., Sect. B*, 2010, **268**, 1818.
46 M. Titze, A. Katzenmeyer, S. Frisone, J. A. Ohlhausen, A. Flores, D. Campbell, B. Li, Y. Wang, J. Han and E. S. Bielejec, *et al.*, *AIP Adv.*, 2024, **14**, 045326.
47 M. Titze, D. L. Perry, E. A. Auden, J. L. Pacheco, J. Abraham and E. S. Bielejec, *J. Vac. Sci. Technol., B*, 2021, **39**, 012802.
48 S. Stoll and A. Schweiger, *J. Magn. Reson.*, 2006, **178**, 42.
49 W. K. Schenken, Y. Liu, L. Krishna, A. A. Majid, C. A. Koh, P. C. Taylor and R. T. Collins, *Phys. Rev. B*, 2020, **101**, 245204.
50 D. Pak, A. Nandi, M. Titze, E. S. Bielejec, H. Alaeian and M. Hosseini, *Commun. Phys.*, 2022, **5**, 89.
51 S. Revesz, A. Misiara, J. B. Abraham, E. S. Bielejec, H. Li and M. Titze, *ACS Photonics*, 2024, **11**, 2221.
52 H.-o Horie, T. Kikudome, K. Teramura and S. Yamanaka, *J. Solid State Chem.*, 2009, **182**, 129.
53 J. R. Dennis and E. B. Hale, *J. Appl. Phys.*, 1978, **49**, 1119.

54 H. Müller, K. Schmid, H. Ryssel and I. Ruge, *Ion Implantation in Semiconductors and Other Materials*, 1973, vol. 203, pp. 203–214.
55 R. J. Schreutelkamp, J. Custer, J. Liefting, W. Lu and F. Saris, *Mater. Sci. Rep.*, 1991, **6**, 275.
56 J. Hubbell, *National Bureau of Standards Report NSRDS-NBS29*, Washington DC, 1969.
57 H. Sigmund and D. Weiss, in Ion Implantation: Equipment and Techniques: Proceedings of the Fourth International Conference Berchtesgaden, *Fed. Rep. of Germany, September 13–17, 1982*, Springer, 1983, pp. 473–480.
58 H. Yahiro, K. Yamaji, M. Shiotani, S. Yamanaka and M. Ishikawa, *Chem. Phys. Lett.*, 1995, **246**, 167.
59 M. Yamaga, T. Kishita, K. Goto, S. Sunaba, T. Kume, T. Ban, R. Himeno, F. Ohashi and S. Nonomura, *J. Phys. Chem. Solids*, 2020, **140**, 109358.
60 J. E. Wertz, P. Auzins, R. Weeks and R. Silsbee, *Phys. Rev.*, 1957, **107**, 1535.
61 L. M. Portsel, V. B. Shuman, A. A. Lavrent'ev, A. N. Lodygin, N. V. Abrosimov and Y. A. Astrov, *Semiconductors*, 2020, **54**, 393.
62 Y. A. Astrov, L. M. Portsel, V. B. Shuman, A. N. Lodygin and N. V. Abrosimov, *Phys. Status Solidi A*, 2022, **219**, 2200463.
63 R. Abraham, A. DeAbreu, K. Morse, V. Shuman, L. Portsel, A. Lodygin, Y. A. Astrov, N. Abrosimov, S. Pavlov and H.-W. Hübers, *et al.*, *Phys. Rev. B*, 2018, **98**, 045202.